applied sciences

MDPI

Article

Inductance Estimation Based on Wavelet-GMDH for Sensorless Control of PMSM

Gwangmin Park [1] and Junhyung Bae [2,*]

[1] Vehicle Electrification R&D Center, Korea Automotive Technology Institute, Guji-myeon, Dalseong-gun, Daegu 43011, Republic of Korea; gmpark@katech.re.kr
[2] Department of Electrical Engineering, Daegu Catholic University, 13-13 Hayang-ro, Hayang-eup, Gyeongsan 38430, Republic of Korea
* Correspondence: baejh80@cu.ac.kr; Tel.: +82-53-850-2764

Abstract: In permanent magnet synchronous motor (PMSM) sensorless drive systems, the motor inductance is a crucial parameter for rotor position estimation. Variations in the motor current induce changes in the inductance, leading to core magnetic saturation and degradation in the accuracy of rotor position estimation. In systems with constant load torque, the saturated inductance remains constant. This inductance error causes a consistent error in rotor position estimation and some performance degradation, but it does not result in speed estimation errors. However, in systems with periodic load torque, the error in the saturated inductance varies, consequently causing fluctuations in both the estimated position and speed errors. Periodic speed errors complicate speed control and degrade the torque compensation performance. In this paper, we propose a wavelet denoising-group method of data handling (GMDH) based method for accurate inductance estimation in PMSM sensorless control systems with periodic load torque compensation. We present a method to analyze and filter the collected three-phase current signals of the PMSM using wavelet transformation and utilize the filtered results as inputs to GMDH for training. Additionally, a method for magnetic saturation compensation using the inductance parameter estimator is proposed to minimize periodic speed fluctuations and improve control accuracy. To replicate the load conditions and parameter variations equivalent to the actual system, experiments were conducted to measure the speed ripples, inductance variations, and torque component of the current. Finally, software simulation was performed to confirm the inductance estimation results and verify the proposed method by simulating load conditions equivalent to the experimental results.

Keywords: permanent magnet synchronous motor (PMSM); sensorless control; wavelet transform; noise reduction; group method of data handling (GMDH); magnetic saturation; inductance estimation

check for updates

Citation: Park, G.; Bae, J. Inductance Estimation Based on Wavelet-GMDH for Sensorless Control of PMSM. *Appl. Sci.* **2024**, *14*, 4386. https://doi.org/10.3390/app14114386

Academic Editors: Miaolei Zhou and Rui Xu

Received: 20 April 2024
Revised: 17 May 2024
Accepted: 21 May 2024
Published: 22 May 2024

Copyright: © 2024 by the authors. Licensee MDPI, Basel, Switzerland. This article is an open access article distributed under the terms and conditions of the Creative Commons Attribution (CC BY) license (https://creativecommons.org/licenses/by/4.0/).

1. Introduction

Due to its advantages such as high efficiency and lightweight design, permanent magnet synchronous motors (PMSMs) are widely used not only in household appliances but also in automotive electric motors. To achieve high performance, field-oriented control (FOC) is predominantly utilized, which requires real-time knowledge of the rotor position. However, practical issues such as installation feasibility, high sensor costs, and control failures in case of sensor malfunctions have led to active research on sensorless control methods for estimating the position and speed of the rotor. Sensorless control techniques mainly consist of two approaches: current model-based methods and extended back electromotive force (EMF) based methods [1–9]. Recently, there has been a significant adoption of extended EMF based methods, which offer unlimited input variables and rapid response capabilities, due to the arctangent operation achievable with microprocessor technology.

In cases where the external load torque remains constant, the torque component current due to magnetic saturation and the error in the inductance parameters remain constant

as well, resulting in a consistent error in rotor position estimation. Such a consistently sized error in the rotor position has minimal impact on the estimation error of the speed. However, in scenarios where periodic load torque occurs, the inductance parameters also exhibit periodic variations, leading to periodic fluctuations in both the position estimation error and speed error. Therefore, in environments where the magnitude and fluctuation rate of the load torque are significant, the changes in inductance, a key parameter in rotor position estimation, become pronounced, leading to increased estimation errors and consequently reduced control precision of the entire system. Particularly in environments directly exposed to external vibrations and loads, such as electric motors near engines and powertrains, pumps, and compressors for household appliances, control performance can degrade sharply. Analyzing the pattern of the external load and applying appropriate compensating currents can mitigate the influences of load torque variations [6,10]. However, implementing such methods may lead to secondary issues such as increased eddy currents due to the increased magnitude of compensating currents, resulting in increased ripples in speed estimation. Without appropriate compensation control considering these factors, mechanical instability and NVH (noise, vibration, and harshness) issues may arise in the overall system. Therefore, accurately estimating the actual size of the inductance and applying real-time closed-loop control can enhance the precision of sensorless speed control.

Efforts have been made to address the issue of magnetic saturation resulting from changes in the inductance by constructing observer-based mathematical models to estimate the value of inductance [11–14]. However, this method relies on the estimated rotor position and speed information obtained in sensorless drive systems, making the estimated inductance size sensitive to variations in back electromotive force constants and drive output voltage changes. Therefore, even with appropriate back electromotive force constants, exposure to periodic load torque fluctuations can degrade the system stability and speed estimation performance due to the occurrence of noise, phase delays, and other factors.

Unlike model-based methods, soft computing methods utilizing data-driven approaches allow for the selection of input variables and define partial expressions of input–output data to objectively predict system equations. This enables more accurate and faster parameter learning and estimation, especially in cases of nonlinear relationships where input–output relationships or model functions are not specific. Particularly, the group method of data handling (GMDH), a form of a self-organizing neural network (SONN), estimates output parameters in the form of polynomial expressions in multilayered structures. GMDH offers fast computation speed, good real-time performance, and excellent accuracy, making it advantageous for embedded systems compared to neural networks, fuzzy algorithms, and others. Due to its flexible structure that evolves through learning, GMDH does not have fixed layer numbers and node counts; instead, it iteratively creates and disbands layers. Furthermore, GMDH effectively reduces parameter estimation errors by combining multiple input-output datasets and dynamically generating and modeling the required set of coefficients [15].

Compared to conventional model-based techniques for estimating the inductance parameters of PMSM sensorless drives, GMDH based estimation offers several key advantages. Firstly, GMDH based learning methods are well suited for complex nonlinear models such as motor systems. By learning a multilayered structure of subexpressions represented in polynomial form, it minimizes the time and cost required for modeling complex nonlinear systems. Secondly, GMDH based learning accurately estimates unknown parameter variables and compensates for delays or distortions, resulting in superior performance compared to other methods in terms of comparative verification and RMS (root mean square) error. Thirdly, the learning process enables easy adaptation to various operational load conditions such as step input loads, periodic loads, random profiles, and more [16–19].

While recent research has highlighted the application of machine learning in motor control systems, attempts to apply machine learning for sensorless control parameter prediction and compensation control are rare due to implementation challenges, optimization

issues, and others. Particularly, applying GMDH based learning techniques to nonlinear systems without appropriately selecting the design parameters can degrade the control characteristics of the system. Moreover, in the presence of unknown disturbances or significant noise in the inputs for machine learning, the estimated results cannot be trusted, and have a negative impact on the system. Therefore, it is necessary not only to design appropriate training parameters suitable for nonlinear sensorless systems but also to perform optimized learning through noise reduction and the refinement of the input data for machine learning.

The combination of wavelet transform for signal analysis and artificial neural networks is increasingly being applied in research. Primarily, studies are conducted where wavelet transform is used for signal analysis to extract feature vectors, followed by the application of artificial neural networks for diagnostics. Wavelet transform is widely used in signal processing and image processing as it removes noise from high-frequency components and enables simultaneous analysis in the time–frequency domain. However, such research is limited to cases applying to physical faults or winding faults in electric motors [20,21]. In addition, there are studies that have integrated wavelets and machine learning such as GMDH to perform load forecasting or failure prediction of power systems [22,23], but no cases have been applied to the parameter estimation of PMSM.

In this paper, we conducted a study on sensorless PMSM drive inductance estimation based on wavelet denoising based machine learning to minimize the rotor position and speed errors and compensate for external periodic torque fluctuations. Firstly, we analyzed the impact of rotor position errors and speed estimation caused by magnetic saturation phenomena induced by external load conditions in extended electromotive force-based sensorless control. To minimize the uncertainty caused by magnetic saturation and improve the real-time control performance, we proposed a method to estimate the inductance of permanent magnet synchronous motors using a wavelet-GMDH algorithm, which combines time–frequency analysis and data-driven methods, and performed compensatory control for magnetic saturation. For reducing estimation errors and improving control precision, we performed optimization learning for the inductance for various load torque patterns. Through the analysis of wavelet transform, the noise classification and reduction of specific signals are conducted without distortion or delay, effectively improving the quality of input signals for GMDH learning. Wavelet noise reduction was used to filter high-frequency outliers in the current data, facilitating the smooth training of the learning algorithm for inductance estimation. Furthermore, to appropriately respond to situations such as unknown disturbances or increasing errors in estimates, we implemented the real-time estimation and monitoring of the position error magnitude. The main contribution of this paper is to estimate the inductance in real time by applying machine learning called GMDH, beyond the simple current signal analysis of motors through wavelet transformations. Moreover, by integrating GMDH with denoising wavelet transform into a sensorless control system, improved control performance can be achieved even under conditions of high noise and severe load.

The structure of this paper is as follows. In Section 2, the sensorless control theory of PMSM and the issues related to magnetic saturation are analyzed. Section 3 presents a mathematical model for wavelet-GMDH based inductance estimation and the proposed method. In Section 4, an algorithm proposed for wavelet-GMDH based compensation control is implemented and modeled using MATLAB R2023a. Finally, in Section 5, we validate the proposed wavelet-GMDH based magnetic saturation compensation method and confirm the results of the control performance through software simulations. To replicate the load conditions and parameter variations equivalent to the actual system, experiments are conducted to measure speed ripples, inductance variations, and the torque component of the current, and the resulting values are incorporated into the simulation as load conditions.

2. Magnetic Saturation of Sensorless Control

Generally, the voltage equations in the *d-q* synchronous frame for the vector control of PMSM is given by

$$\begin{bmatrix} v_d \\ v_q \end{bmatrix} = \begin{bmatrix} R_a + pL_d & -\omega L_q \\ \omega L_q & R_a + pL_d \end{bmatrix} \begin{bmatrix} i_d \\ i_q \end{bmatrix} + \begin{bmatrix} 0 \\ \omega\psi \end{bmatrix}, \tag{1}$$

where R_a, ψ, and p are the stator resistance, the back EMF constant, and a differential operator, respectively.L_d, L_q, v_d, v_q, and i_d, i_q are the inductances, the stator voltages, and currents in the *d-q* synchronous reference frame, respectively.

Ignoring the difference between the estimated speed and the actual speed, Equation (1) can be converted to the γ-δ axes estimated by the extended back EMF. Then, the voltage equation can be represented as [1]

$$\begin{bmatrix} v_\gamma \\ v_\delta \end{bmatrix} = \begin{bmatrix} R_a + pL_d & -\omega L_q \\ \omega L_q & R_a + pL_d \end{bmatrix} \begin{bmatrix} i_\gamma \\ i_\delta \end{bmatrix} + \begin{bmatrix} e_\gamma \\ e_\delta \end{bmatrix}, \tag{2}$$

where $e_\gamma = -E_{ex} sin\theta_e, e_\delta = -E_{ex} cos\theta_e$, and $E_{ex} = \omega\left[\left(L_d - L_q\right)i_d + \psi\right] - \left(L_d - L_q\right)\frac{di_q}{dt}$.

v_γ, v_δ, i_γ, i_δ, and e_γ, e_δ represent the stator voltages, the currents, and the extended back EMFs in the γ-δ estimated synchronous reference frame, respectively, accounting for the rotor position error. Utilizing e_γ and e_δ, the rotor position error can be calculated as

$$\hat{\theta}_e = tan^{-1}\left(-\frac{\hat{\theta}_\gamma}{\hat{\theta}_\delta}\right) \cong -\frac{\hat{e}_\gamma}{E_{ex}}. \tag{3}$$

As shown in Figure 1, the estimated speed $\hat{\omega}_r$ can be obtained through a PI controller with the estimated rotor position error $\hat{\theta}_e$ as the input and a low-pass filter for noise reduction. Moreover, the estimated rotor position $\hat{\theta}$ can be obtained by integrating the estimated speed.

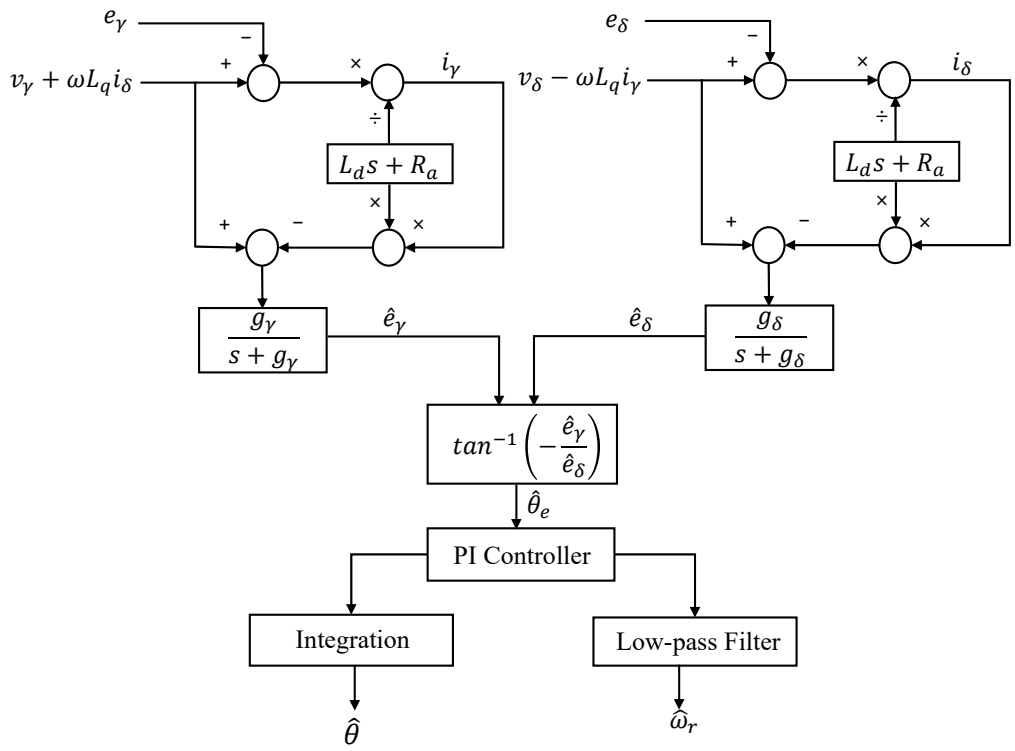

Figure 1. Block diagram of extended EMF based sensorless control algorithm.

Ensuring precise sensorless control requires accurately determining parameters such as the resistance and inductance, as represented in Equation (2). In systems affected by significant periodic loads, like those in pumps or compressors, the discrepancy between the actual q-axis inductance (L_q) and the estimated q-axis inductance ($\hat{L}_q$) due to magnetic saturation leads to inaccuracies in the estimated rotor position. Consequently, to address the deviations resulting from magnetic saturation between the actual and estimated values, Equation (2) can be rearranged for the extended back EMF e_γ, e_δ as

$$\begin{bmatrix} e_\gamma \\ e_\delta \end{bmatrix} = \begin{bmatrix} v_\gamma \\ v_\delta \end{bmatrix} - \begin{bmatrix} R_a + pL_d & -\omega\hat{L}_q \\ \omega\hat{L}_q & R_a + pL_d \end{bmatrix} \begin{bmatrix} i_\gamma \\ i_\delta \end{bmatrix} + \begin{bmatrix} \Delta e_\gamma \\ \Delta e_\delta \end{bmatrix}, \tag{4}$$

where $\Delta e_\gamma = -p\Delta L_d i_\gamma + \omega\Delta L_q i_\delta$, and $\Delta e_\delta = -p\Delta L_d i_\delta - \omega\Delta L_q i_\gamma$.

Note that ΔL_d and ΔL_q are the errors of the d- and q-axes inductance, which are the value obtained by subtracting the estimated inductance from the actual inductance.

e_γ and e_δ increase or decrease due to the influence of Δe_γ and Δe_δ including the inductance error, in a practical system. As a result, the rotor position error and speed ripple increase.

The estimated position errors corresponding to the variation in the γ-δ axes extended back EMF are illustrated in Figure 2. Note that $\hat{\theta}'_e$, $\hat{\theta}''_e$, E'_{ex}, and E''_{ex} represent the estimated rotor position error and extended EMF, caused by the γ- and δ-axes extended back EMF errors (Δe_γ, Δe_δ), respectively. As shown in Figure 2a, in the case of a constant value of the γ- and δ-axes extended back EMF, e_γ and e_δ, the estimated extended EMF E_{ex} aligns with the q-axis of the synchronous reference frame. In Figure 2b,c, on the other hand, when errors occur in the γ-δ axes extended back EMF resulting from an inductance variation, it leads to the generation of estimated rotor position errors. Usually, the δ-axis extended back EMF component exhibits a significantly greater magnitude compared to the γ-axis component ($e_\delta \gg e_\gamma$); therefore, the variation in the γ-axis extended back EMF component significantly influences the speed estimation error compared to the δ-axis component [14]. Consequently, $\hat{\theta}'_e$ is significantly larger than $\hat{\theta}''_e$ compared to $\hat{\theta}_e$, when the magnitudes of Δe_γ and Δe_δ are the same value, as shown in Figure 2b,c.

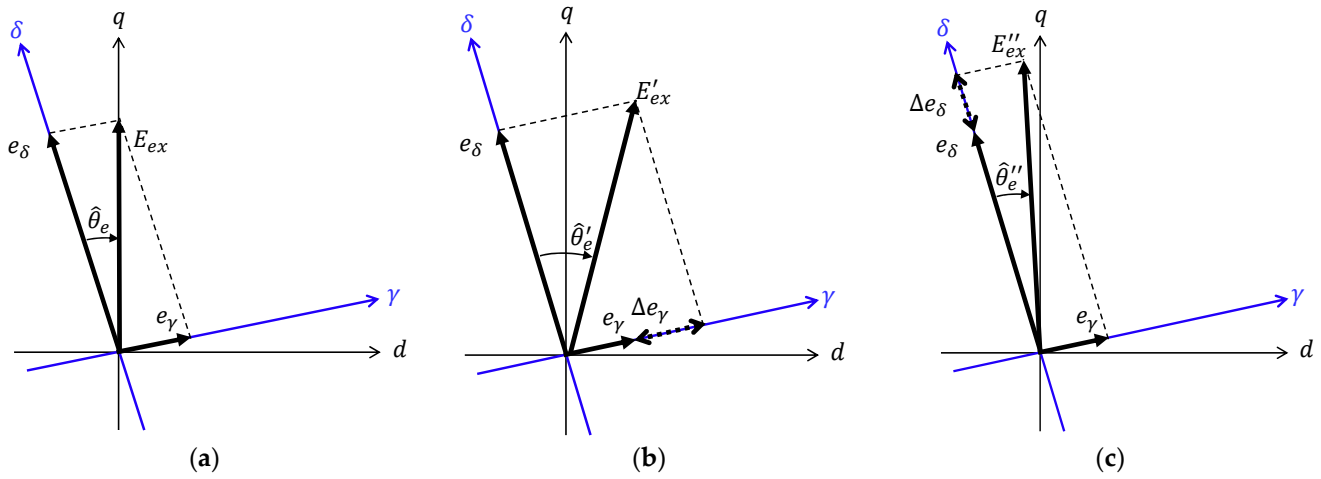

Figure 2. Comparison of estimated position errors (**a**) without extended back EMF errors, (**b**) with γ-axis extended back EMF error (Δe_γ), and (**c**) δ-axis extended back EMF error (Δe_δ).

In addition, to compare the magnitude of the two terms constituting the γ-axis back EMF variation Δe_γ in Equation (4), a simulation result of the comparison of $\omega\hat{L}_q i_\delta$ and $p\hat{L}_d i_\gamma$ under the condition of periodic load torque is represented in Figure 3. The term $\omega\hat{L}_q i_\delta$ including the q-axis inductance is the main component in e_γ estimation; hence, it can be expressed as $\Delta e_\gamma \approx \omega\Delta L_q i_\delta$. Consequently, since the dominant factor affecting position error estimation is $\omega\Delta L_q i_\delta$, compensating fluctuations in the q-axis inductance, being the

principal parameter influenced by magnetic saturation, can effectively enhance both the position error and speed ripple.

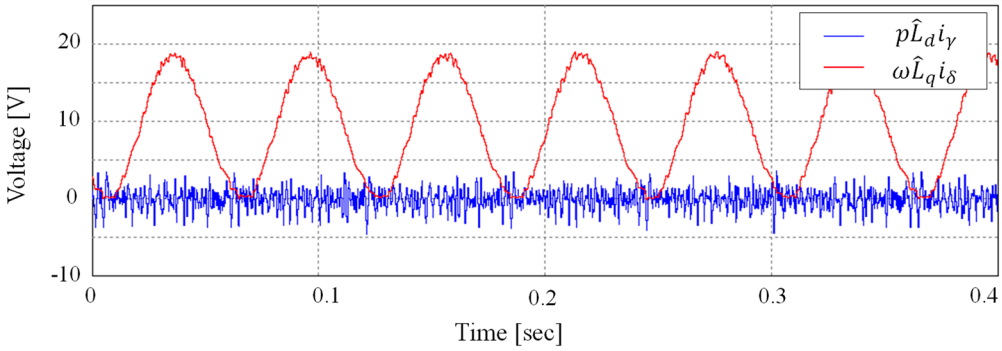

Figure 3. Comparison of $\omega\hat{L}_q i_\delta$ and $p\hat{L}_d i_\gamma$, where $\omega = 1000$ rpm, $\hat{L}_d = 1.5$ mH, and $\hat{L}_q = 2$ mH.

3. Wavelet-GMDH Based Inductance Estimation Method

3.1. Signal Denoising via Discrete Wavelet Transform

The wavelet transform was initially introduced by Grossman and Morlet [24] and was primarily employed for the evaluation of seismic data. Wavelets offer advantages over traditional Fourier methods when analyzing signals containing discontinuities and sharp spikes. Most data analysis applications utilize the continuous-time wavelet transform (CWT), providing an affine-invariant time-frequency representation. However, the discrete wavelet transform (DWT) is the most well-known version due to its outstanding signal compaction properties across various real-world signal classes, along with its computational efficiency. Additionally, the implementation of the DWT is straightforward as it relies on perfect reconstruction filter banks, as well as upsampling and downsampling techniques.

The DWT translates continuous-time functions into a set of numbers [25].

$$c_{j,k} = \left\langle x(t), \varphi_{j,k}(t) \right\rangle = \int x(t)\varphi_{j,k}(t)dt \tag{5}$$

$$d_{j,k} = \left\langle x(t), \psi_{j,k}(t) \right\rangle = \int x(t)\psi_{j,k}(t)dt, \tag{6}$$

where $x(t)$ is a real function, $\varphi_{j,k}(t)$ is the scaling function, and $\psi_{j,k}(t)$ is the wavelet function.

In the DWT, the coefficients $c_{j,k}$ are referred to as the smooth or approximation coefficients, while the coefficients $d_{j,k}$ are termed the detail or wavelet coefficients. The inverse DWT is given by

$$x(t) = \sum_k c_{j,k}\varphi_{j,k}(t) + \sum_{j=J}^{\infty}\sum_k d_{j,k}\psi_{j,k}(t), \tag{7}$$

where J is the starting index, typically equal to zero. The DWT decomposes a given signal $x(t)$ into its constituent components $c_{j,k}$ and $d_{j,k}$. The inverse DWT reconstructs the signal $x(t)$ from its constituent components $c_{j,k}$ and $d_{j,k}$.

Indeed, the wavelet transform has demonstrated its efficiency in noise removal tasks. It offers an effective method to eliminate noisy components from received signals. The DWT typically proceeds in three phases; in the first phase, the input signal function is decomposed into piecewise functions, each composed of a wavelet and a coefficient. These wavelets are orthogonal to one another and collectively form an orthonormal basis. Furthermore, small coefficients typically represent noise, while large coefficients correspond to significant features within the received signal. Hence, in the second phase, the DWT approach filters these coefficients to retain the most significant ones. This phase is often referred to as thresholding, as any coefficient with a value below a defined threshold is discarded. Finally, the signal is reconstructed by computing the inverse DWT using the filtered coefficients.

There has been extensive research into noise removal in signals using wavelet transform. A significant contribution is the work of Donoho and Johnstone [25,26], which focuses on the thresholding of wavelet coefficients and subsequent reconstruction.

The model of a noisy signal $r(n)$ may be written as

$$r(n) = s(n) + e(n), \tag{8}$$

where $s(n)$ represents the original signal and $e(n)$ represents the noise. A wavelet transform of the above equation yields the relation:

$$W_r = W_s + W_e, \tag{9}$$

where the vector W_r corresponds to the wavelet coefficients of the noisy signal, W_s contains the wavelet coefficients of the original signal, and W_e represents the noise wavelet coefficients. After applying a threshold τ, the modified wavelet coefficients $W_{r\tau}$ of the degraded signal can be obtained. The inverse wavelet transform of $W_{r\tau}$ yields the restored signal. Choosing the value of the threshold is a fundamental problem to prevent oversmoothing or undersmoothing. The most well-known threshold estimation methods include the SURE threshold method and the universal threshold method. The SURE estimator as a threshold is given by [27]

$$\text{SURE}(\tau) = T(\tau) + \frac{N - 2N_0}{N}\sigma^2 \tag{10}$$

$$T(\tau) = \frac{1}{N}\|W_{r\tau} - W_r\|, \tag{11}$$

where

$T(\tau)$ represents the SURE estimator as a threshold;
N is the total number of wavelet coefficients;
N_0 is the number of coefficients that were replaced by zeros; and
σ^2 is the noise variance.

However, the optimal choice of the threshold depends on the noise energy present. The universal threshold, as described in [28], is

$$\tau = \sqrt{2logN}\sigma, \tag{12}$$

which uses the noise energy explicitly and selects a threshold proportional to σ. The noise variance σ^2 at each level j is estimated using the following robust estimator:

$$\sigma_j^{-2} = \frac{MAD(|W_{rj}|)}{0.6745}, \tag{13}$$

where MAD represents the median absolute deviation from 0, and the factor 0.6745 is chosen for calibration with the Gaussian distribution.

In the case of hard thresholding, the estimated coefficients will be [29,30]

$$W_{r\tau} = \begin{cases} W_r \; if \; |W_r| \geq \delta \\ 0, \; otherwise \end{cases}. \tag{14}$$

In the case of soft thresholding, the estimated coefficients will be

$$W_{r\tau} = \begin{cases} W_r - \delta \; if \; W_r \geq \delta \\ 0 \; if \; |W_r| \leq \delta \\ W_r + \delta \; if \; W_r \leq -\delta \end{cases}. \tag{15}$$

3.2. Group Method of Data Handling (GMDH)

Model-based inductance estimation utilizes the same motor dynamics variables with extended EMF sensorless control. This leads to a partial contradiction in the response speed

of the estimated rotor position and inductance, resulting in a time delay. However, the machine learning approach employing the GMDH algorithm predicts a system equation by selecting input variables, segmenting input-output variables, and defining partial expressions. As a result, despite the nonlinear relationship between input–output variables or the unspecified function type of the model, hierarchically combining partial expressions enables obtaining the estimation equation accurately without time delays. Thus, machine learning based on the GMDH algorithm can be seamlessly integrated into an embedded system. The GMDH algorithm is comprised of a layered network with a specific structure honed during training. It not only captures nonlinear dynamics via a mathematical model but also encompasses higher-order polynomials, thus ensuring stability. The sophisticated relationship between input and output variables can be illustrated through a complex polynomial series reminiscent of the Kolmogorov–Gabor polynomial [15]:

$$y = a_0 + \sum_{i=1}^{m} a_i x_i + \sum_{i=1}^{m} \sum_{j=1}^{m} a_{ij} x_i x_j + \sum_{i=1}^{m} \sum_{j=1}^{m} \sum_{k=1}^{m} a_{ijk} x_i x_j x_k + \cdots, \quad (16)$$

where x, y, m, and a represent the input into the system, the output of each regression layer, the number of inputs, and a coefficient, respectively.

A GMDH algorithm can serve as a predictor for estimating the output of nonlinear complex systems, applicable to most scenarios represented by quadratic forms of input variables. The output of each quadratic neuron is calculated as

$$y(x_1, x_2) = a_0 + a_1 x_1 + a_2 x_2 + a_3 x_1^2 + a_4 x_2^2 + a_5 x_1 x_2, \quad (17)$$

where $a_i (i = 0, 1, \ldots, 5)$ are the weight coefficients of the quadratic neuron to be learned. The coefficients a_i are derived from linear regression analysis and a recursive algorithm, which iteratively minimizes errors when validating data at each layer.

To train a GMDH network with inputs, it is essential to consider the combinations of all possible input pairs. A system of Gaussian normal equations must be solved to determine the coefficients for each model. The coefficient of nodes in each layer can be represented by [15–17]

$$\boldsymbol{A} = \left(\boldsymbol{X}^T \boldsymbol{X}\right)^{-1} \boldsymbol{X}^T \boldsymbol{Y}$$

where

$$\begin{gathered} \boldsymbol{Y} = [y_1, y_2, \cdots, y_m]^T, \\ \boldsymbol{A} = [a_0, a_1, a_2, a_3, a_4, a_5], \\ \boldsymbol{X} = \begin{bmatrix} 1 & x_{1p} & x_{1q} & x_{1p}x_{1q} & x_{1p}^2 & x_{1q}^2 \\ 1 & x_{2p} & x_{2q} & x_{2p}x_{2q} & x_{2p}^2 & x_{2q}^2 \\ \vdots & \vdots & \vdots & \vdots & \vdots & \vdots \\ 1 & x_{mp} & x_{mq} & x_{mp}x_{mq} & x_{mp}^2 & x_{mq}^2 \end{bmatrix}. \end{gathered} \quad (18)$$

Therefore, the output of each polynomial can be calculated as

$$\boldsymbol{Y} = \boldsymbol{A} \times \boldsymbol{X}. \quad (19)$$

To assess the adequacy of the partial description of the validation dataset, the linear regression index R_k is obtained as

$$R_k = \sqrt{\frac{\sum_{i=1}^{n} (y_i - g_i)^2}{\sum_{i=1}^{n} y_i^2}}, k = 1, 2, \cdots \frac{1}{2} m(m-1). \quad (20)$$

In addition, to evaluate how well a regression model fits a dataset, it is necessary to compute the RMSE (root mean square error). This metric indicates the average deviation between the predicted values from the model and the actual values in the dataset.

The RMSE can be calculated as

$$RMSE = \sqrt{\frac{\sum(y_i - \hat{y}_i)^2}{N}}, \quad (21)$$

where $\hat{y}_i$ is the predicted value for the ith observation, and N is the number of observations.

The main function of GMDH involves the forward propagation of a signal through the network nodes, similar to the principle utilized in typical neural networks. Every layer comprises simple nodes, each executing its own polynomial transfer function and transmitting its output to the nodes in the subsequent layer.

4. Implementation of Wavelet-GMDH Based Compensation Control

Using wavelet transformation, feature vectors of PMSM three-phase current sensor signals were extracted and high-frequency noise removed, and machine learning was performed based on the refined data. In addition, using the estimated inductance data using the wavelet-GMDH technique, the magnetic flux saturation state of the actual system was accurately calculated, and control was performed by generating a compensation signal in real time. As shown in Table 1, the wavelet scaling function, decomposition level, denoising method, and threshold rule were designed, considering the frequency and noise level of the input sensor signals.

Table 1. Wavelet transform parameters.

Parameter	Value
Wavelet scaling function	sym4
Decomposition level	8
Denoising method	universal threshold
Threshold rule	soft

Since the input signal comprises the three-phase current signal of the PMSM, including noise such as the measurement noise and power noise, utilizing it directly as the input signal for GMDH can adversely affect the quality and accuracy of the machine learning output data. Therefore, appropriate signal processing is necessary. Especially in severe load conditions with a noisy environment, the signal-to-noise ratio of the sensor increases. This becomes a major factor in deteriorating speed ripples and control stability of the system caused by magnetic saturation.

Figure 4 represents the simulation results of the raw signal of the three-phase current sensor and the denoised signal after applying the wavelet filter, respectively, under the condition of periodic load torque. As shown in Figure 4a, the measured signal from the current sensors contains noise, including measurement noise and power switching noise, in the original signal. However, by applying wavelet transformation, small wavelet coefficients are classified as noise and selectively removed, resulting in minimal distortion or delay in the signal, thus not affecting the quality of the original signal. Finally, after applying a threshold to the wavelet coefficients and using wavelet inverse transformation, the restored original data are shown in Figure 4b.

Machine learning regression was performed utilizing the GMDH algorithm, incorporating multi-input polynomials comprising refined sensor signals, overvoltage, and input current control reference signals. The design parameters for the GMDH based machine learning were determined as the input variables, maximum number of neurons in a layer, maximum number of layers, and training ratio. The number of layers was set to five or more, with a training ratio of 80%, accounting for the computational speed of the processor and the magnitude of the RMS error. To enhance the compensation control performance for periodic loads, training was conducted under various periodic input conditions characterized by different frequencies and loads.

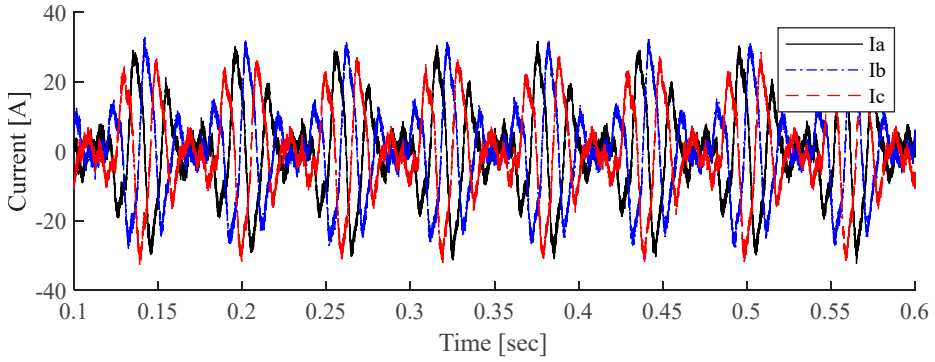

(**a**)

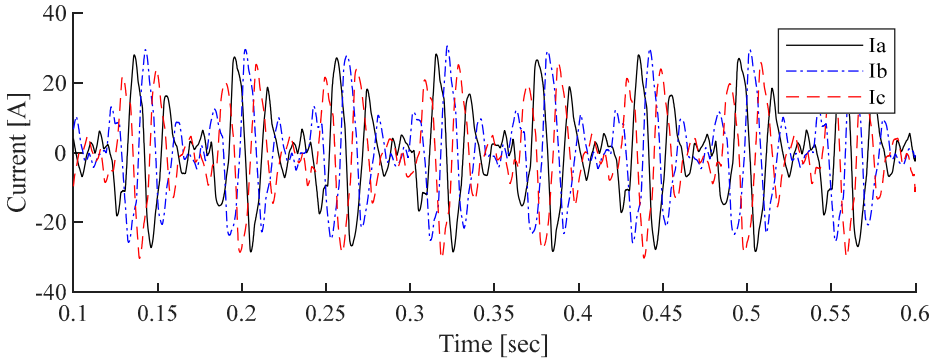

(**b**)

Figure 4. Comparison of three-phase current signals. (**a**) Raw signals without a wavelet filter; (**b**) denoised signals with a wavelet filter.

Table 2 presents a comparison of the RMSE, mean squared error (MSE), mean absolute error (MAE), and the linear regression index (R and R^2) of the *q*-axis inductance, estimated by wavelet-GMDH based learning for each case of input variables and regression layers using MATLAB R2023a. Furthermore, the comparisons of the evaluation metrics (RMSE, MSE, MAE) for all cases are shown in Figure 5. As a result of the comparison, it is observed that the evaluation metrics results are improved as the number of input variables and regression layers increase. Based on the analysis results, the optimal regression combination chosen consisted of eight input variables with five layers (Case 5), satisfying the training performance criteria (RMS error < 1, linear regression index (R) > 0.99), from Equations (20) and (21). Additionally, both the MSE and MAE were observed to be less than 0.6%, and the coefficient of determination was close to 1, indicating the good performance of the regression model. To further minimize errors, the number of regression layers can be increased to seven or more, but it leads to an increase in the processor load due to the complex computation.

Table 2. Comparison of training results for *q*-axis inductance.

Case	Input Variables	No. of Layers	RMSE (%)	MSE (%)	MAE (%)	Linear Regression Index	
						R	R^2
1	I_a, I_b, I_c, $V_{d.ref}$, $V_{q.ref}$	5 layers	1.8077	3.2678	1.4462	0.9865	0.9732
2		7 layers	1.76658	3.1208	1.4124	0.9872	0.9746
3	I_a, I_b, I_c, $V_{d.ref}$, $V_{q.ref}$, I_{ds}, I_{qs}	5 layers	1.3414	1.7994	1.0672	0.9926	0.9853
4		7 layers	1.2722	1.6185	1.0195	0.9934	0.9868
5	I_a, I_b, I_c, $V_{d.ref}$, $V_{q.ref}$, I_{ds}, I_{qs}, I_{q_ref}	5 layers	0.6278	0.3941	0.5004	0.9984	0.9968
6		7 layers	0.6105	0.3727	0.4877	0.9985	0.9970

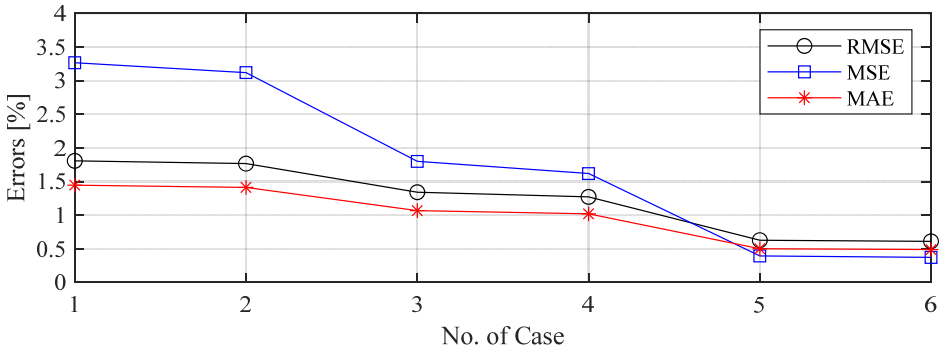

Figure 5. Comparisons of evaluation metrics (RMSE, MSE, MAE) for all cases.

Figure 6 presents the linear regression results, histogram of the estimation errors, and estimation errors of the wavelet-GMDH simulation for case 5 comprising eight input variables with five layers. As shown in Figure 6a, the slope of the fitting line in the linear regression is close to 1. In Figure 6b, analysis of the error histogram indicates that the error values exhibit characteristics of a normal distribution based on a zero-mean, indicating the robustness of the trained model across the dataset. Furthermore, the estimation errors, directly related to the RMSE, MSE, and MAE, appear relatively uniform, with the mean value remaining below 1%, as shown in Figure 6c.

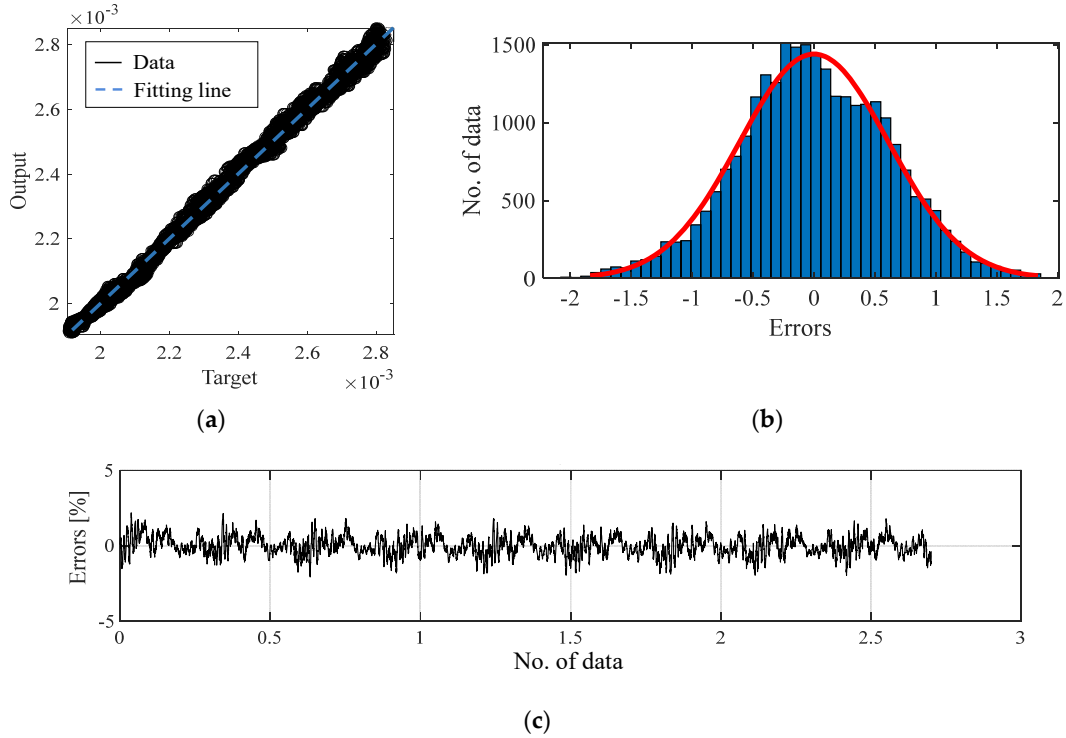

Figure 6. Wavelet-GMDH based training results. (**a**) Linear regression result; (**b**) histogram of estimation errors; (**c**) estimation errors.

5. Simulation Results

5.1. System Modeling

Figure 7 represents the block diagram of the entire control system for the PMSM sensorless control, including the proposed wavelet-GMDH based magnetic saturation compensation control. Through an optimized polynomial expression-based numerical model utilizing the GMDH algorithm, real-time calculation of the inductance is achieved from eight input variables, including phase currents, voltage references, etc. In the magnetic saturation compensation block, the variation in the estimated inductance ΔL_q is utilized to

compute the extended back EMF fluctuation. Subsequently, the back EMF fluctuation $\Delta\hat{e}_\gamma$ is fed back to the sensorless position controller to compensate for the inductance variation in real time and mitigate the speed ripple.

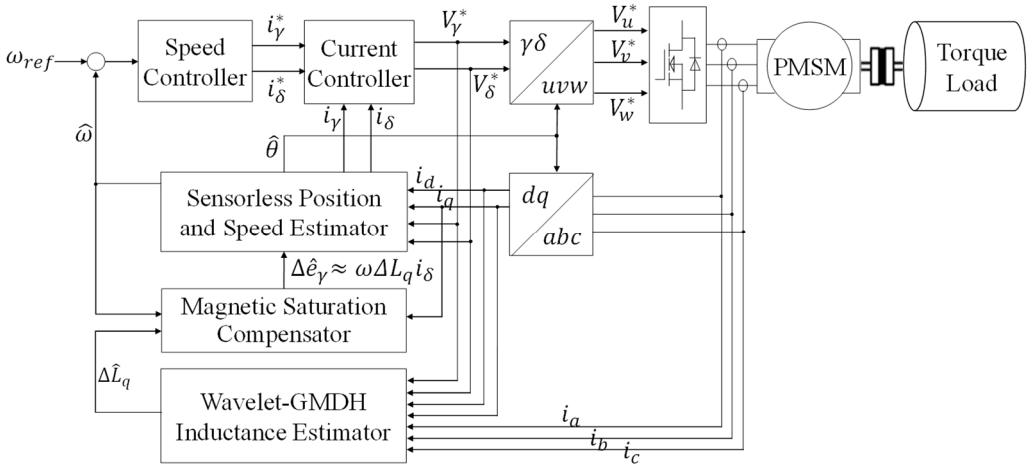

Figure 7. Block diagram of the sensorless compensation control system based on wavelet-GMDH.

In this paper, simulations were conducted using PSIM v.11.1 to analyze and compare the performance of inductance estimation and speed ripple compensation using magnetic saturation compensation methods. As shown in Table 3, motor parameters equivalent to commercial motor specifications, such as resistance and the number of pole pairs/slots, were applied to simulate the real system.

Table 3. Motor parameters.

Parameter	Value	Unit
Rated power	3	kW
DC link voltage	400	V
Winding resistance	0.3	Ω
Number of poles	6	-
Number of slots	27	-
d-axis inductance	1.5	mH
q-axis inductance	2.0	mH

Figure 8 represents the sensorless control system modeled for the application of a magnetic saturation and compensation control system in a simulation. It is implemented as a dual motor system and consists of a sensorless motor drive and a load motor system to simulate periodic loads. The electric motor model provided by the PSIM v11.1 inherently does not account for magnetic saturation. Therefore, a detailed motor model based on mathematical models and motor parameters was implemented. Furthermore, to create an environment similar to the actual system for the wavelet-GMDH based magnetic saturation compensation algorithm, a microcontroller unit (MCU) controller was modeled through co-simulation with a DLL file based on C language programming.

In systems exposed to severe load conditions, such as components near engines and powertrains, pumps, and compressors, periodic load torque can be compensated through a PMSM load torque compensator. However, the magnetic saturation, driven by the increasing compensation current, undermines the precision of sensorless speed control and load torque compensation. Assuming that the frequency and magnitude of the periodic load torque are predictable, the δ-axis compensation current depending on the load is expressed as the sum of the frequency component with constant amplitude I_S and DC offset I_{DC} [16]:

$$i_\delta = I_S sin\omega t + I_{DC}, \quad (22)$$

where i_δ is the δ-axis compensation current, and ω is the frequency component of the rotor speed. The γ-axis compensation current is obtained from the δ-axis compensation current according to the maximum torque per ampere rule. With accurate rotor position estimation, even in the presence of inductance variation, the periodic load torque can be effectively compensated.

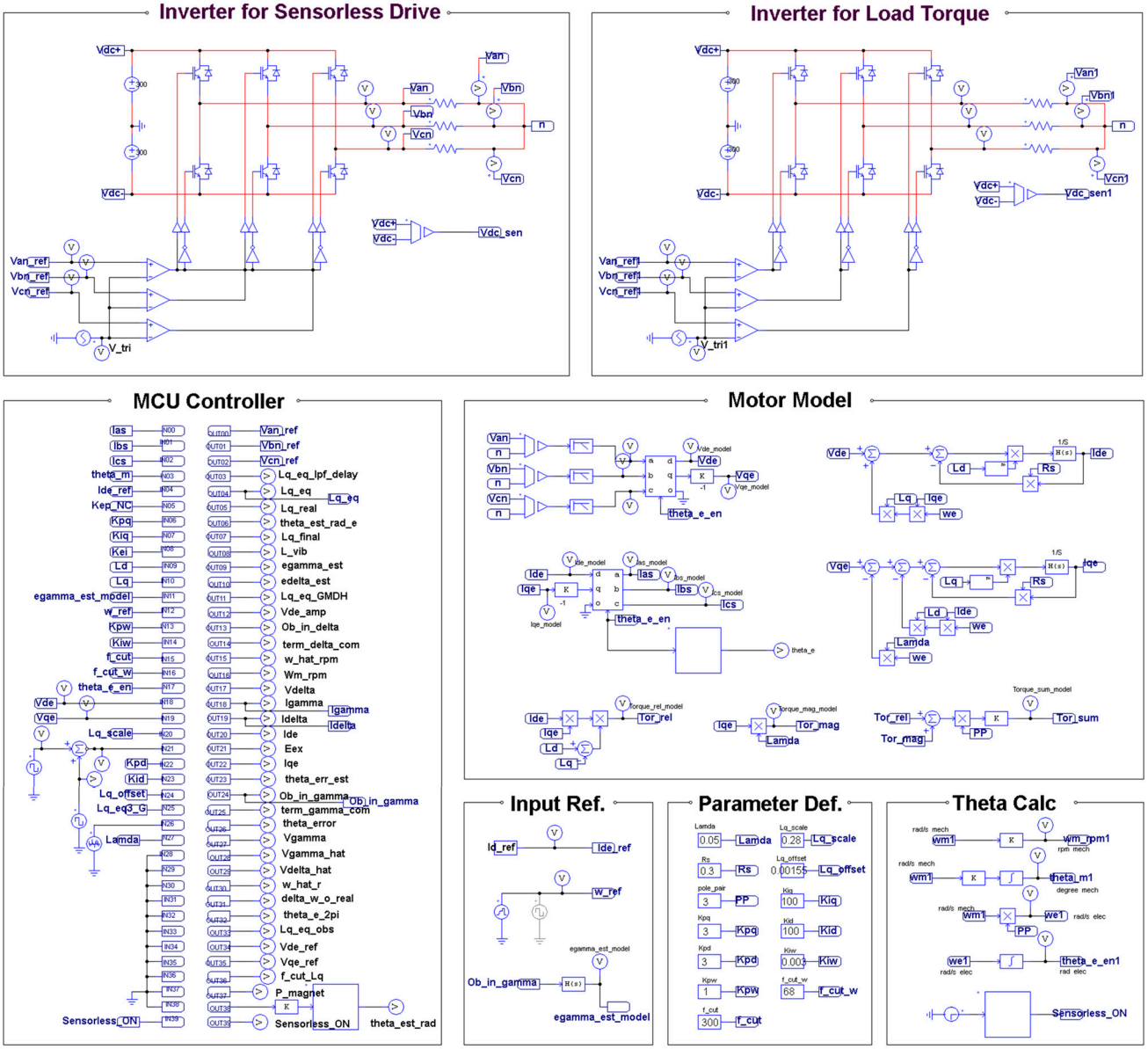

Figure 8. Simulation model for magnetic saturation compensation of sensorless control system.

5.2. Simulation Results

Figure 9 presents the experimental results of the q-axis inductance, speed error, and theta error caused by the load torque compensation current, i_δ, during constant speed operation at 1000 rpm in a motor drive system. From the results in Figure 9b, it can be observed that the inductance variation during magnetic saturation due to periodic loads showed significant fluctuations of approximately $\pm 50\%$ compared to the normal condition. In addition, as seen in Figure 9c,d, in the condition of magnetic saturation, the speed error ripple reached a maximum of 120 rpm to -150 rpm, and the angle error was over 25 degrees. Based on the experimental results, the simulation modeling of sensorless motor control was conducted to correlate with actual signals such as the magnetic saturation magnitude and speed ripple according to the load torque compensation current.

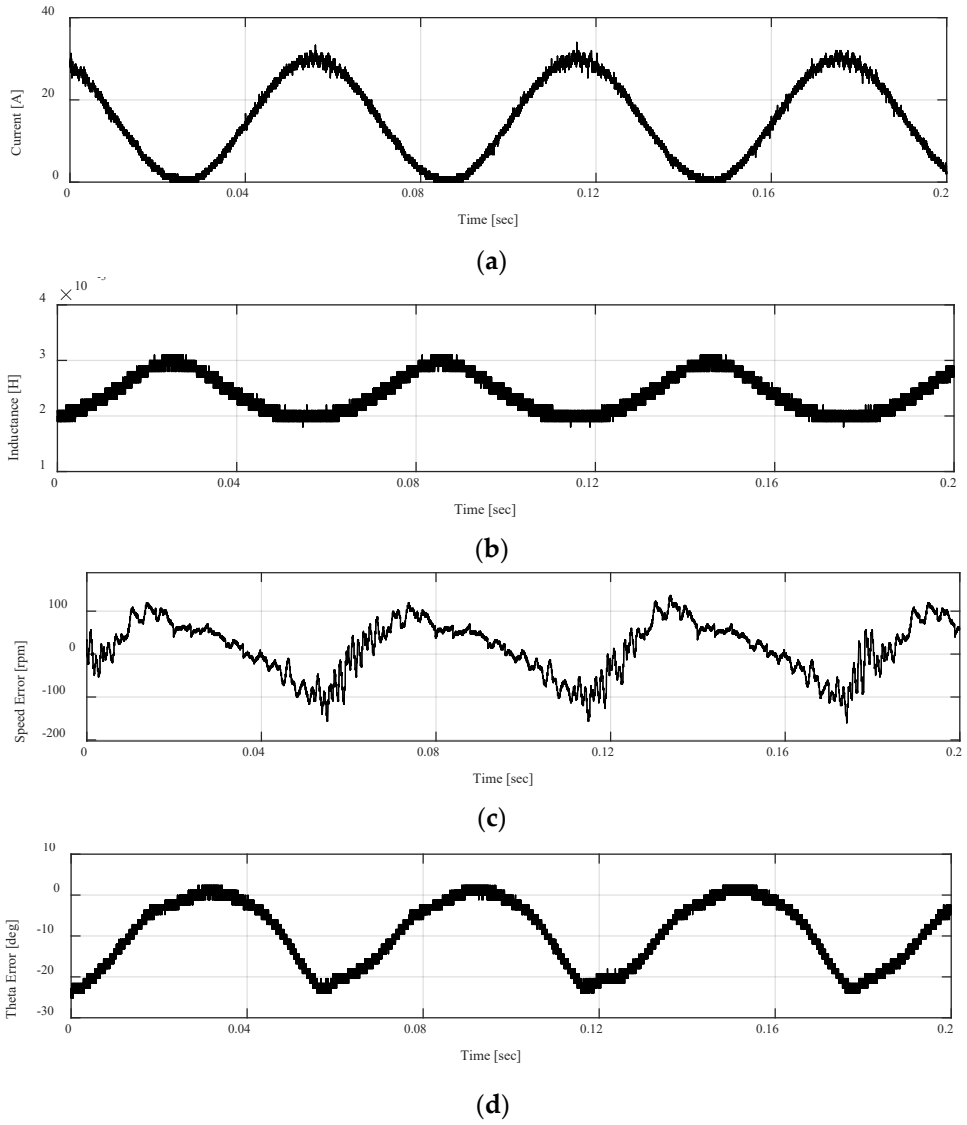

Figure 9. Experimental results when the motor operated at 1000 rpm with a periodic load torque for (**a**) δ-axis current, (**b**) q-axis inductance, (**c**) speed error, and (**d**) theta error.

Figure 10 shows the simulation results of the torque compensation current, inductance, and speed performed by simulating the equivalent load conditions as the experimental results. When the δ-axis current is controlled with a peak-to-peak amplitude of 30 A in Figure 10a, the actual inductance fluctuates, as depicted in Figure 10b. Conducting control without compensating for the inductance variations due to magnetic saturation leads to significant ripple in the estimated speed, as shown in Figure 10c.

Figure 11 represents the comparison of the estimated speed between no compensation, GMDH based compensation, and wavelet-GMDH based compensation in the time domain when operating at a constant speed of 1000 rpm under conditions of magnetic saturation. It shows the results obtained when basic sensorless control is performed without compensation, as well as when magnetic saturation compensation control is applied based on the GMDH algorithm and wavelet-GMDH algorithm, respectively. The estimated speed error displays peak-to-peak ripples of over $\pm$100 rpm when compensation control is not applied. On the other hand, when GMDH based compensation is applied, the ripple is reduced by half, and when wavelet-GMDH based compensation is applied, it is reduced to less than $\pm$30 rpm.

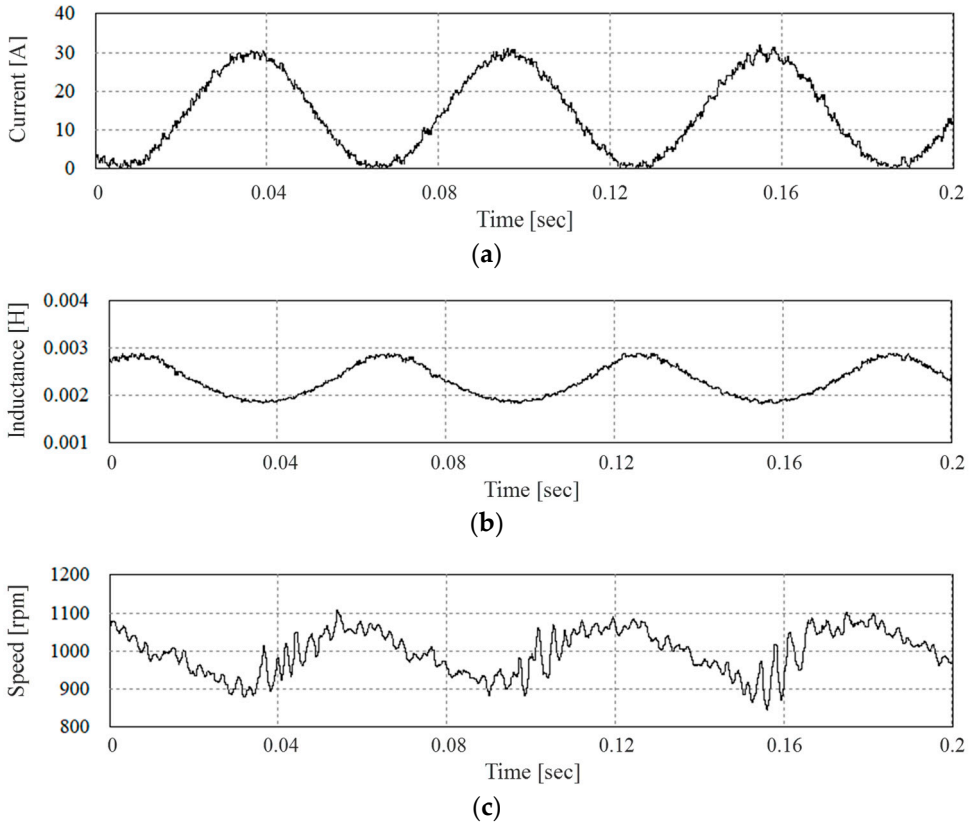

Figure 10. Simulation results when the motor operated at 1000 rpm with a periodic load torque for (**a**) δ-axis current, (**b**) q-axis inductance, and (**c**) estimated speed.

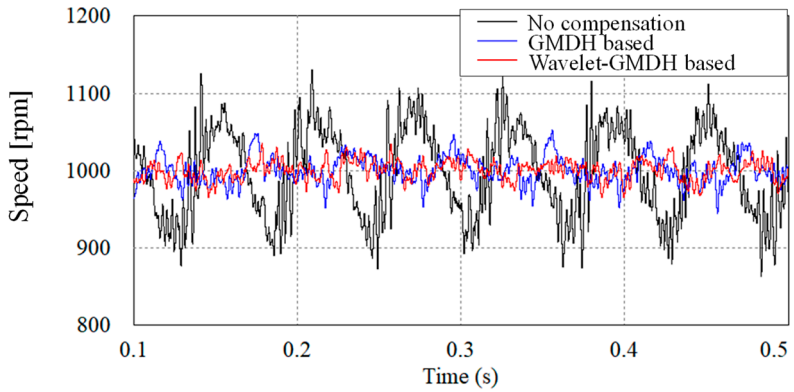

Figure 11. Comparison of estimated speed between no compensation, GMDH based compensation, and wavelet-GMDH based compensation in time domain.

Furthermore, in the frequency domain comparison results, as depicted in Figure 12, prior to the application of compensation control, the amplitude of the first harmonic component, which has the greatest influence on the speed ripple, was significantly large at about 80 rpm. In the case of GMDH, the amplitude of the first harmonic of the speed reduced to 1/7th compared to the uncompensated condition. On the other hand, after applying the proposed compensation control, it was observed that the amplitude decreased to less than 10 rpm, representing a significant improvement over GMDH. Particularly, as the frequency increases, the amplitudes of the second and third harmonic frequency components are nearly eliminated.

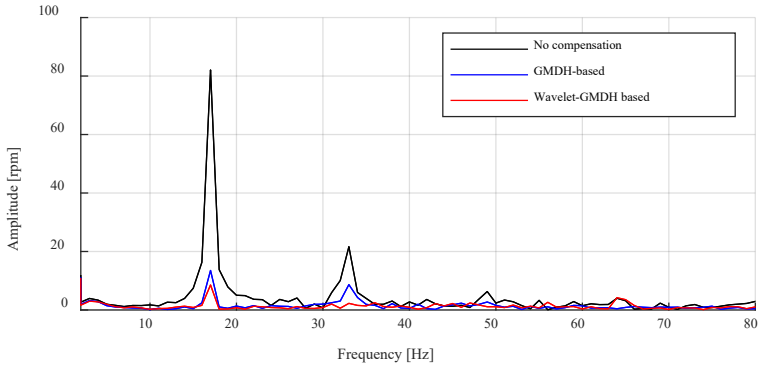

Figure 12. Comparison of estimated speed between no compensation, GMDH based compensation, and wavelet-GMDH based compensation in frequency domain.

Figure 13 shows the comparison of the torque ripple between the case without compensation and the case with compensation based on the wavelet-GMDH under conditions of magnetic flux saturation, identical to the previous load condition. By compensating for magnetic saturation, not only is the estimated speed error reduced, but it has also been observed that the magnitude of the motor's torque ripple decreases by more than 5%.

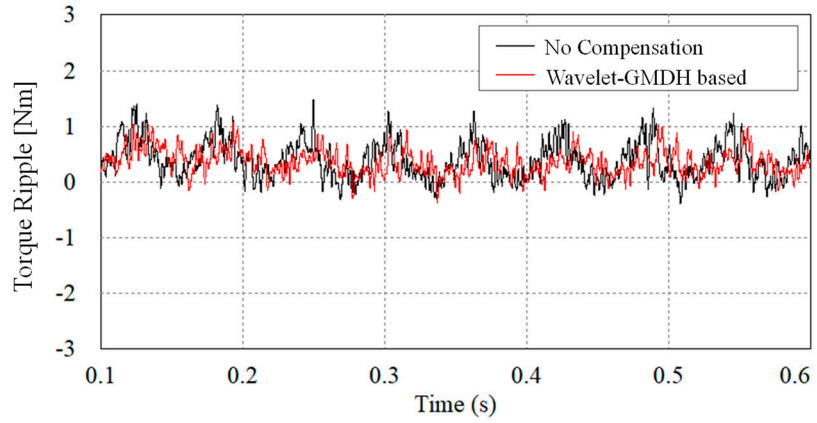

Figure 13. Comparison of torque ripple between no compensation and wavelet-GMDH based compensation.

6. Conclusions

The inductance variation due to magnetic saturation causes fluctuations in both the estimated position and speed, consequently degrading the accuracy of sensorless control. This paper proposes a wavelet-GMDH based method for accurately estimating the inductance in PMSM sensorless control systems with periodic load torque compensation.

Through the analysis of wavelet transform levels and feature vectors extraction, the noise classification and reduction of three-phase current signals were achieved without distortion or delay, effectively improving the quality of the input signals for GMDH learning. We designed and implemented an optimized training model for nonlinear sensorless control systems based on wavelet-GMDH, utilizing a polynomial-based machine learning approach, with denoised input variables through wavelet transform.

In the simulation and analysis results, it was observed that when applying the GMDH based magnetic saturation compensation under severe load torque fluctuations, the speed ripples were reduced by half compared to the case without compensation control. In contrast, when applying the wavelet-GMDH, it was confirmed that the speed ripples were significantly reduced to less than 1/3 due to the accuracy enhancement resulting from the noise reduction and optimized training. Furthermore, by applying the proposed algorithm to nonlinear systems with uncertainties such as sensorless control, we validated that the control performance can be efficiently improved compared to conventional compensation methods. In particular, by employing GMDH with denoising wavelet transform to improve

the training accuracy, it was confirmed that high-precision control can be achieved even in situations with high noise and severe load conditions.

The proposed methodology was evaluated through offline testing using simulated data obtained by replicating the measured load conditions. By applying the proposed method and analyzing external load patterns, it is feasible to reduce the real-time impact of load torque variations in motor systems directly exposed to various external vibrations and loads, such as components near powertrains, industrial pumps, etc.

However, to enable online testing in the future, further research in various aspects is required. To obtain sufficient sensor data and perform fast parameter estimation calculations, hardware configuration requires current sensors with high sampling rates and computational devices offering fast processing speeds. Furthermore, advanced research into real-time algorithm refinement should be conducted concurrently.

Author Contributions: Conceptualization, G.P. and J.B.; methodology, G.P. and J.B.; software, G.P.; validation, G.P. and J.B.; formal analysis, G.P. and J.B.; investigation, G.P. and J.B.; resources, G.P.; data curation, G.P.; writing—original draft preparation, G.P.; writing—review and editing, J.B.; visualization, G.P.; supervision, J.B.; project administration, J.B.; funding acquisition, J.B. All authors have read and agreed to the published version of the manuscript.

Funding: This work was supported by research grants from Daegu Catholic University in 2022. (Research Project No. 20221119).

Institutional Review Board Statement: Not applicable.

Informed Consent Statement: Not applicable.

Data Availability Statement: The datasets presented in this article are not readily available because a unique asset of the university to which the corresponding author belongs. Requests to access the datasets should be directed to the Industry Academic Cooperation Foundation, Daegu Catholic University.

Conflicts of Interest: The authors declare no conflicts of interest.

References

1. Morimoto, S.; Kawamoto, K.; Sanada, M.; Takeda, Y. Sensorless control strategy for salient-pole PMSM based on extended EMF in rotating reference frame. *IEEE Trans. Ind. Appl.* **2002**, *38*, 1054–1061. [CrossRef]
2. Hoai, H.-K.; Chen, S.-C.; Chang, C.-F. Realization of the Neural Fuzzy Controller for the Sensorless PMSM Drive Control System. *Electronics* **2020**, *9*, 1371. [CrossRef]
3. Mizutani, R.; Takeshita, T.; Matsui, N. Current model-based sensorless drives of salient-pole PMSM at low speed and standstill. *IEEE Trans. Ind. Appl.* **1998**, *34*, 841–846. [CrossRef]
4. Zhou, C.; Yu, F.; Zhu, C.; Mao, J. Sensorless Predictive Current Control of a Permanent Magnet Synchronous Motor Powered by a Three-Level Inverter. *Appl. Sci.* **2021**, *11*, 10840. [CrossRef]
5. Zhu, Y.; Tao, B.; Xiao, M.; Yang, G.; Zhang, X.; Lu, K. Luenberger Position Observer Based on Deadbeat-Current Predictive Control for Sensorless PMSM. *Electronics* **2020**, *9*, 1325. [CrossRef]
6. Lee, K.W.; Ha, J.I. Evaluation of back-EMF estimators for sensorless control of permanent magnet synchronous motors. *J. Power Electron.* **2012**, *12*, 604–614. [CrossRef]
7. Meng, K.; Liu, Q.; Zhang, Z.; Wu, H.; Feng, H.; Kang, T. Sensorless HSPMSM Control of an Improved SMC and EKF Based on Immune PSO. *Appl. Sci.* **2023**, *13*, 12407. [CrossRef]
8. Wang, D.; Liu, X. Sensorless Control of PMSM with Improved Adaptive Super-Twisting Sliding Mode Observer and IST-QSG. *IEEE Trans. Transp. Electr.* **2024**. [CrossRef]
9. Yang, Y.; Liu, X. A Novel Nonsingular Terminal Sliding Mode Observer-Based Sensorless Control for Electrical Drive System. *Mathematics* **2022**, *10*, 3123. [CrossRef]
10. Cho, K.Y. Sensorless control for a PM synchronous motor in a single piston rotary compressor. *J. Power Electron.* **2006**, *6*, 29–37.
11. Hasegawa, M.; Matsui, K. Position sensorless control for interior permanent magnet synchronous motor using adaptive flux observer with inductance identification. *IET Electron. Power Appl.* **2009**, *3*, 209–217. [CrossRef]
12. Ichikawa, S.; Tomita, M.; Doki, S.; Okuma, S. Sensorless control of permanent-magnet synchronous motors using online parameter identification based on system identification theory. *IEEE Trans. Ind. Electron.* **2006**, *53*, 363–371. [CrossRef]
13. Lin, H.; Hwang, K.Y.; Kwon, B.I. An Improved Flux Observer for Sensorless Permanent Magnet Synchronous Motor Drives with Parameter Identification. *J. Electron. Eng. Technol.* **2013**, *8*, 516–523. [CrossRef]

14. Underwood, S.J.; Husain, I. Online Parameter Estimation and Adaptive Control of Permanent-Magnet Synchronous Machines. *IEEE Trans. Ind. Electron.* **2010**, *57*, 2435–2443. [CrossRef]
15. Farlow, S. *Self-Organizing Methods in Modeling: GMDH Type Algorithms*; CRC Press: Boca Raton, FL, USA, 1984; pp. 8–86.
16. Park, G.; Kim, G.; Gu, B.-G. Sensorless PMSM Drive Inductance Estimation Based on a Data-Driven Approach. *Electronics* **2021**, *10*, 791. [CrossRef]
17. Pandya, A.S.; Gilbar, T.; Kim, K.B. Neural Network Training Using a GMDH Type Algorithm. *Int. J. Fuzzy Logic Intell. Syst.* **2005**, *5*, 52–58. [CrossRef]
18. Guo, H.; Sagawa, S.; Watanabe, T.; Ichinokura, O. Sensorless driving method of permanent-magnet synchronous motors based on neural networks. *IEEE Trans. Magn.* **2003**, *39*, 3247–3249.
19. Iwasaki, M.; Takei, H.; Matsui, N. GMDH-based modeling and feedforward compensation for nonlinear friction in table drive systems. *IEEE Trans. Ind. Electron.* **2003**, *50*, 1172–1178. [CrossRef]
20. Heydarzadeh, M.; Zafarani, M.; Nourani, M.; Akin, B.A. Wavelet-Based Fault Diagnosis Approach for Permanent Magnet Synchronous Motors. *IEEE Trans. Energy Conv.* **2019**, *34*, 761–772. [CrossRef]
21. Vinayak, B.A.; Anand, K.A.; Jagadanand, G. Wavelet-based real-time stator fault detection of inverter-fed induction motor. *IET Electron. Power Appl.* **2019**, *14*, 82–90. [CrossRef]
22. Koo, B.G.; Lee, H.S.; Park, J. Short-term Electric Load Forecasting Based on Wavelet Transform and GMDH. *J. Electr. Eng. Technol.* **2015**, *10*, 832–837. [CrossRef]
23. Stefanon, S.F.; Ribeiro, M.H.D.M.; Nied, A.; Mariani, V.C.; Coelho, L.S.; Rocha, D.F.M.; Grebogi, R.B.; Ruano, A.E.B. Wavelet group method of data handling for fault prediction in electrical power insulators. *Int. J. Electron. Power Energy Syst.* **2020**, *123*, 106269. [CrossRef]
24. Grossmann, A.; Morlet, J. Decomposition of Hardy Functions into Square Integrable Wavelets of Constant Shape. *SIAM J. Math. Anal.* **1984**, *15*, 723–736. [CrossRef]
25. Donoho, D.L.; Johnstone, I.M. Adapting to unknown smoothness via wavelet shrinkage. *J. Am. Stat. Assoc.* **1993**, *90*, 1200–1224. [CrossRef]
26. Donoho, D.L.; Johnstone, I.M. Ideal spatial adaptation via wavelet shrinkage. *Biometrika* **1994**, *81*, 425–455. [CrossRef]
27. Johnstone, I.M.; Silverman, B.W. Wavelet threshold estimators for data with correlated noise, J.R. *Stat. Soc.* **1997**, *59*, 319–351. [CrossRef]
28. Yinyu, G.; Kim, N.H. Image Denoising Using Adaptive Threshold Method in Wavelet Domain. *Int. J. Inf. Commun. Eng.* **2011**, *9*, 763–768.
29. Halidou, A.; Mohamadou, Y.; Ari, A.A.A.; Zacko, E. Review of wavelet denoising algorithms. *Multimed. Tools Appl.* **2023**, *82*, 41539–41569. [CrossRef]
30. Donoho, D.L. Denoising by soft thresholding. *IEEE Trans. Inf. Theory* **1995**, *41*, 613–627. [CrossRef]

Disclaimer/Publisher's Note: The statements, opinions and data contained in all publications are solely those of the individual author(s) and contributor(s) and not of MDPI and/or the editor(s). MDPI and/or the editor(s) disclaim responsibility for any injury to people or property resulting from any ideas, methods, instructions or products referred to in the content.